Journal of
Materials Chemistry A

COMMUNICATION

View Article Online
View Journal | View Issue

Cite this: J. Mater. Chem. A, 2025, 13, 27093

Received 30th June 2025
Accepted 29th July 2025

DOI: 10.1039/d5ta05287d

rsc.li/materials-a

Systematic design of safe, high-energy lithium-ion batteries by merging intercalation and alloying anodes

Spencer A. Langevin, Courtney A. McHale, Tanner Hamann and Jesse S. Ko *

The development of advanced anode materials is critical for enhancing the energy density and safety of lithium-ion batteries (LIBs). Here, we demonstrate a blended anode comprising lithium titanate (LTO) and tin–antimony (SnSb) alloy, investigating the trade-offs between capacity and cycle life across varying LTO : SnSb ratios. The near-zero strain properties of LTO provide mechanical durability by mitigating the volume expansion issues of SnSb when present at levels <20 wt% in the blended anode. This system delivers a favorable half-cell potential (~0.5–1.5 V *vs.* Li/Li$^+$) and specific capacities ranging from 300 to 500 mAh g^{-1}.

The selection of anode materials for lithium-ion batteries (LIBs) is not as diverse as that of cathode materials. Alloying anodes represent a promising advancement for electrochemical energy storage, offering the potential to significantly enhance battery performance and safety.[1–5] Traditional LIBs commonly use graphite (gr) as the anode material due to its low half-cell potential, electrochemical stability during lithium intercalation, and high gravimetric and volumetric energy densities (267 Wh kg^{-1} and 763 Wh L^{-1}, respectively).[6,7] However, graphite's relatively low theoretical capacity when compared to alloying anodes, such as silicon (Si), tin (Sn), and antimony (Sb), has driven efforts into exploring alternative anode materials.[1–8] Oxide-based anode materials have also emerged as a promising material, offering improved performance and safety.[9–12] Oxide-based anodes, such as titanium dioxide (TiO_2),[13–16] lithium titanate ($Li_4Ti_5O_{12}$; LTO),[9,10,17–19] titanium niobate ($TiNb_xO_{2+2.5x}$; TNO),[20–22] and niobium oxide (Nb_2O_5),[11,23–25] offer several advantages over conventional graphite anodes. Notably, their higher half-cell potential makes them more resistant to lithium dendrite growth, a major cause of short circuits and battery failures.[9–11] Therefore, the pursuit of energy-dense and safe anode materials remains critical for advancing LIB technology.

Presently, Si anodes dominate anode materials research, owing to its high theoretical capacity (3580 mAh g^{-1} for $Li_{15}Si_4$ at room temperature), natural abundance, and low half-cell potential (~0.37 V *vs.* Li/Li$^+$).[26–29] However, the large volume expansion of Si (300%) and poor electrical conductivity has led to challenges in commercialization.[26–29] To compensate for these shortcomings, the concept of blending Si with gr (Si/gr) as a composite anode has gained significant traction in an attempt to combine the advantageous properties of gr (high electrical conductivity and structural stability) with Si (high theoretical capacity).[30–34] This composite anode is designed to allow gr to act as a mechanically-stable matrix and provide a porous network that accommodates Si volume expansion, successfully improving cycle life.[29,30,32–34] Though Si/gr has merits in terms of energy density, the low half-cell potentials still pose a safety concern due to the potential for lithium dendrite growth.

As an alternative to Si/gr anode composites, we propose an alternative selection of blended anode materials—such as combining oxide-based anodes and Sn- and Sb-based alloying anodes[5,35,36]—as a unique approach to bridging a critical gap in materials selection (Fig. 1; 0.5–1.5 V *vs.* Li/Li$^+$ and 350–600 mAh g^{-1}).[37] Extensive research has been conducted on titanate and niobate anode materials, which have demonstrated high-rate capability and enhanced safety; yet, their specific capacities are typically limited to <300 mAh g^{-1}. Similarly, Sb, Sn, and SnSb intermetallic alloys have shown significant improvements over Si in terms of electrical conductivity, yet their cycle life remains a challenge.[5] To achieve an optimum balance between half-cell potential (>0.5 V *vs.* Li/Li$^+$) and specific capacity (~300–500 mAh g^{-1}), we demonstrate that systematically blending LTO with SnSb (LTO : SnSb) results in an energy-dense anode material with improved cycle life. In addition, replacing the copper current collector for aluminum leads to lower cost and the potential for zero-volt storage. Given that LTO is a near-zero strain material,[18,19,38] incorporating it into a conductive carbon matrix provides mechanical support for SnSb's volume expansion, thereby improving structural stability. Though prior studies have investigated composites comprising LTO with Si,[39]

Research and Exploratory Development Department, Johns Hopkins University Applied Physics Laboratory, Laurel, MD 20723, USA. E-mail: Jesse.Ko@jhuapl.edu

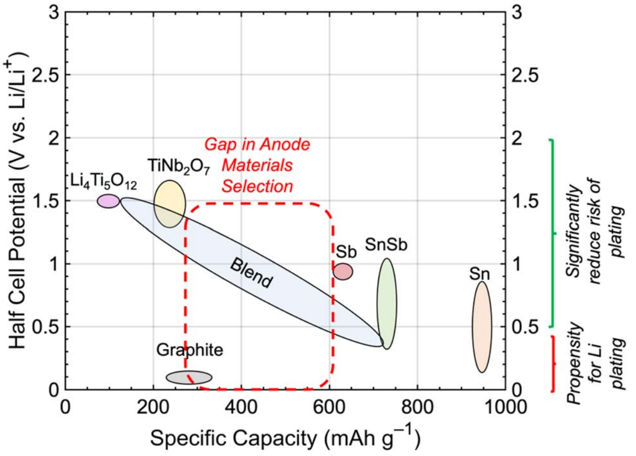

Fig. 1 Schematic illustration of the half-cell potential *versus* specific capacity of select anode materials (*i.e.*, commonly utilized): $Li_4Ti_5O_{12}$, $TiNb_2O_7$, graphite, Sb, SnSb, and Sn. This illustration also presents the potential for blends to mend a critical gap in anode materials selection in terms of their potential and specific capacity, coupled with reference to safety that shows the propensity for lithium plating or reduction in risk.

or Sn,[40,41] a rigorous in-depth assessment that balances capacity and cycle life has yet to be reported. Moreover, SnSb, which offers innately greater cycle life *versus* Sn or Sb alone,[42] has not been previously incorporated as a composite anode with LTO.

While strategies such as nanoporosity,[43–45] hierarchical structures,[46–48] and nanowires[49–52] have improved cycle life for alloying anodes, their complex synthesis routes present significant barriers to integration into current manufacturing techniques like roll-to-roll coating and calendaring. Moreover, Luo *et al.* critically evaluated the impact of inter- and intra-particle porosity in alloying anodes (*e.g.*, Si), emphasizing that careful engineering of inter-particle porosity is required to achieve high gravimetric and volumetric energy densities without compromising cycle life.[53] Beyond compositional optimization, the blending of LTO and SnSb in this work demonstrates a path toward practical performance while maintaining compatibility with standard lithium-ion battery manufacturing processes (*e.g.*, coating and calendaring), providing a technologically-relevant implementation approach that can facilitate industry adoption with existing infrastructure.

The primary criterion for constructing high-capacity blended anodes was to first ensure phase purity of the selected alloying (SnSb) and intercalation (LTO) materials. Rietveld refinement of the X-ray diffraction patterns for SnSb and LTO confirm their phase purity, with all primary reflections closely matching their respective reference patterns (Fig. 2), as indicated by their low-profile residual goodness-of-fit factor (R_{wp} < 10%). To further characterize the materials, scanning electron microscopy (SEM) was performed to analyze the particle sizes of SnSb and LTO. The average particle size for SnSb was estimated to be 5–20 μm, while LTO exhibited primary particle sizes of ~20 μm and secondary particle sizes of ~0.5 μm. Of note, though this is beyond the scope of this work, we hypothesize that smaller nanoparticles incorporated with micron-sized LTO particles will further improve the structural rigidity of the composite anode by further minimizing inter-particle porosity.[53] These two materials were then mixed in several mass ratios (wt : wt), which are denoted as the following: (i) 100 wt% LTO (10 : 0); (ii) 90 wt% LTO and 10 wt% SnSb (9 : 1); (iii) 80 wt% LTO and 20 wt% SnSb (8 : 2); (iv) 50 wt% LTO and 50 wt% SnSb (5 : 5); (v) 30 wt% LTO and 70 wt% SnSb (3 : 7); and (vi) 100 wt% SnSb (0 : 10). Based on these ratios between LTO and SnSb (ranging from 1 : 9 to 9 : 1), the projected specific energies range between 147–282 Wh kg^{-1} (Fig. S1; projections were based on an areal capacity of 3.3 mAh cm^{-2} for the anode, 3.0 mAh cm^{-2} for the $LiNi_{0.8}Co_{0.15}Al_{0.05}O_2$

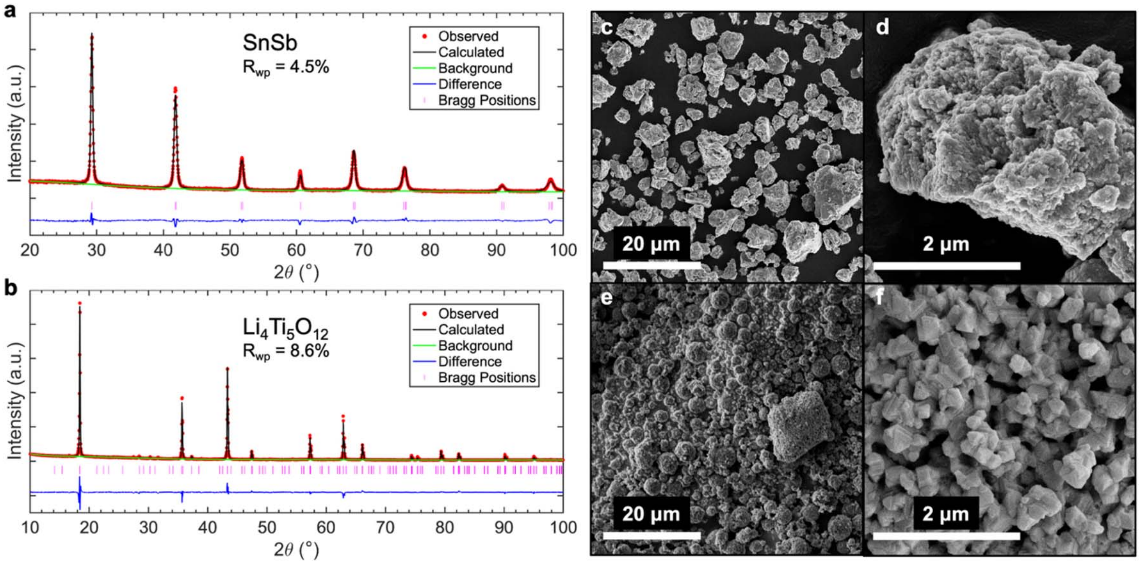

Fig. 2 Rietveld-refined X-ray diffraction patterns of (a) SnSb and (b) $Li_4Ti_5O_{12}$ (LTO) revealing profile residual (R_{wp}) factors < 10%, indicating phase-pure materials. Scanning electron micrographs (SEM) of (c and d) SnSb particles and (e and f) $Li_4Ti_5O_{12}$ particles at both low- and high-magnification, respectively.

Table 1 Summary of half-cell electrochemical properties (average discharge potential and discharge capacity) of LTO : SnSb electrodes with the following ratios: 10 : 0, 9 : 1, 8 : 2, 7 : 3, 5 : 5, 3 : 7, 0 : 10 (wt : wt LTO : SnSb)

LTO : SnSb mass ratio (wt : wt)	Average discharge potential (V *vs.* Li/Li$^+$)	C/10 capacity (mAh g^{-1})	C/5 capacity (mAh g^{-1})	C/2 capacity (mAh g^{-1})	1C capacity (mAh g^{-1})	2C capacity (mAh g^{-1})
10 : 0	1.55	167.9	167.6	166.8	164.6	159.9
9 : 1	1.14	252.5	248.6	239.0	230.7	222.3
8 : 2	0.93	344.7	340.0	327.1	325.3	306.7
7 : 3	0.80	456.9	454.5	437.5	431.2	402.1
5 : 5	0.73	552.0	550.7	528.5	508.8	482.3
3 : 7	0.67	689.0	684.4	656.6	630.6	598.1
0 : 10	0.64	748.1	700.7	621.6	570.6	531.2

(NCA) cathode, and an electrolyte overfill of 60%, in a 5 Ah pouch cell form factor). These formulations were prepared as carbon-composite anodes utilizing active material, conductive carbon, and polymeric binder coated onto aluminum foil. After calendaring, the final electrode thickness for all coatings was measured to be ~60 μm with a porosity of ~40%.

Half-cell electrochemical measurements were conducted using lithium metal as both the reference and counter electrodes to evaluate the average half-cell potential and specific capacities of the blended anodes (Table 1). As expected, LTO (10 : 0) exhibits an average discharge potential of 1.55 V *vs.* Li/Li$^+$ with a C/10 specific capacity of 167.9 mAh g^{-1}, while SnSb (0 : 10) displays a 0.64 V average potential and a capacity of 748.1 mAh g^{-1} (Fig. 3a). LTO demonstrates excellent high-rate capability, with only a 5% capacity loss after increasing to 2C (159.9 mAh g^{-1}). In contrast, SnSb experiences a 29% capacity drop at to 2C (531.2 mAh g^{-1}) due to the slower kinetics of the alloying reaction. With increasing amounts of SnSb in the LTO : SnSb blend, the charge–discharge voltage profiles (Fig. 3a, overlays in Fig. S2) reveal a gradual increase in blended anode capacity, accompanied by a commensurate decrease in average discharge potential. The 9 : 1 blend maintains a slightly lower discharge potential than LTO (1.14 V) while increasing total anode capacity to 252.5 mAh g^{-1} at C/10, with high capacity retention when cycling at 2C (222 mAh g^{-1}). For the 8 : 2 blend, the discharge potential drops ~200 mV (0.93 V), and capacity increases to 344.7 mAh g^{-1} at C/10, retaining 89% capacity at 2C (306.7 mAh g^{-1}). The 7 : 3 ratio exhibits strong capacity retention at a 0.80 V average discharge potential, with 456.9 mAh g^{-1} at C/10 and 402.1 mAh g^{-1} at 2C. For the higher SnSb loadings (5 : 5 and 3 : 7), the average discharge potentials decrease to 0.73 V and 0.67 V, respectively, with specific capacities ranging from 552–689 mAh g^{-1}, though rate performance decreases by over 15% when cycling at 2C. Rate capability overlays of specific

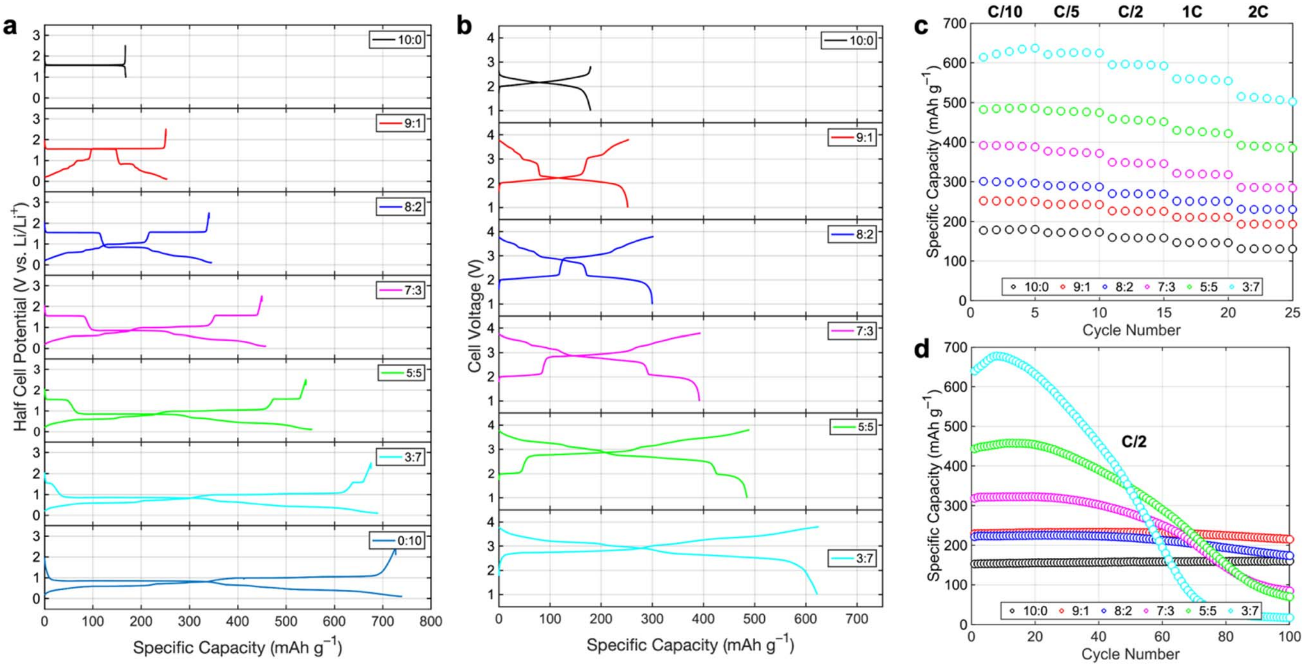

Fig. 3 (a) Half-cell charge–discharge voltage profiles for this series of blended anode materials: 10 : 0, 9 : 1, 8 : 2, 7 : 3, 5 : 5, 3 : 7, 0 : 10 (wt : wt LTO : SnSb). (b) Full-cell charge–discharge voltage profiles (blended anodes paired with NCA cathode); (c) rate capability for full cells with an imposed C-rate ranging from C/10 to 2C; (d) and long-term cycling tests conducted at C/2 for 100 cycles for this series of blended anode materials: 10 : 0, 9 : 1, 8 : 2, 7 : 3, 5 : 5, 3 : 7.

capacity *versus* cycle number for this material series are shown in Fig. S3. Based on these half-cell performance metrics, we then fabricated full cells pairing these anodes with technologically-relevant NCA cathodes to assess practical cell voltage, rate capability, and device-level performance.

Full cells were tested within a voltage range of 1.0–2.8 V for LTO||NCA (10 : 0||NCA) and 1.0–3.8 V for 9 : 1||NCA, 8 : 2||NCA, 7 : 3||NCA, 5 : 5||NCA, and 3 : 7||NCA, optimizing both anode and cathode performance based on their respective half-cell potential windows. The potential window for the LTO : SnSb||NCA cells were determined first by evaluating a range of upper charge voltages (3.6, 3.8, and 4.0 V; Fig. S4) using 7 : 3||NCA as a representative cell, which showed that 1.0 to 3.8 V was ideal for maintaining good capacity retention. Subsequently, the N : P ratio was determined by evaluating two ratios (~0.8 and ~1.1), and ~0.8 was selected, as this showed better capacity retention (Fig. S5). As shown in Fig. 3b (direct overlays are shown in Fig. S6), the 10 : 0||NCA full cell exhibits a characteristic charge–discharge profile with an average discharge voltage of 2.11 V and a C/10 capacity of 180.5 mAh g^{-1} (Table 2). Unlike the near-constant capacities observed in half-cell testing, the 10 : 0||NCA full cell shows a modest capacity drop at 2C (131 mAh g^{-1}) due to the rate limitations of the NCA cathode (Fig. 3c). With increasing SnSb content, the average discharge voltage proportionally increases, accompanied by variations in discharge capacity (Fig. 3b and Table 2). The 9 : 1||NCA full cell achieves a capacity of 250.6 mAh g^{-1} at C/10 with an average discharge voltage of 2.43 V, retaining 193.4 mAh g^{-1} at 2C. The 8 : 2||NCA full cell achieves 296.1 mAh g^{-1} at C/10, maintaining 230.7 mAh g^{-1} at 2C. The 7 : 3||NCA full cell follows this trend with improved capacity and rate retention. For higher SnSb loadings, performance trends begin to shift, and the 5 : 5||NCA full cell exhibits a high C/10 capacity of 485.9 mAh g^{-1}, but capacity retention drops significantly at 2C (384.6 mAh g^{-1}). The 3 : 7||NCA full cell achieves the highest C/10 capacity (637.3 mAh g^{-1}) and 502.6 mAh g^{-1} at 2C; however, it also indicates the greatest capacity fade when cycled at C/2 for 100 cycles (Fig. 3d). For full cells using LTO : SnSb blended anodes with medium-to-high SnSb content (*i.e.*, 5 : 5 to 8 : 2), long-term cycling stability at C/2 collapses at ~60 cycles. The 8 : 2||NCA full cell exhibits only modest degradation at 60 cycles, suggesting this ratio was the upper limit for SnSb incorporation to balance cycle life with discharge capacity. In contrast, both the 9 : 1||NCA and 10 : 0||NCA full cells maintains excellent capacity retention over 100 cycles at C/2, attributed to reduced volume expansion and pulverization of SnSb. Based on the average discharge voltage and C/10 capacities for this series of LTO : SnSb full cells, specific energy metrics were calculated normalizing to both the total anode and cathode mass (not including mass of current collectors, electrolyte and packaging). These estimates show that achievable specific energy values range between 213.5 to 453.3 Wh kg^{-1} at the materials level; yet, we note that ~60% of this value should be taken as a closer approximation towards technological relevance (see also Fig. S1 on projections that incorporate the mass of all cell components, packaging and electrolyte fill).

To investigate the mechanisms behind capacity fade in these blended anode materials, d*Q*/d*V* analyses were performed to track changes in peak intensities and voltage locations, which indicate electrochemical reactions leading to degradation.[54–57] By converting the charge–discharge profiles into d*Q*/d*V* plots at cycle 5 and 100 for this series of blended anode materials, distinct trends emerge based on the LTO : SnSb ratio. For the 10 : 0||NCA full cell, the d*Q*/d*V* peak intensity and broadness remain unchanged between cycles 5 and 100, indicating stable performance with no signs of LTO anode degradation (Fig. S7). In contrast, the 9 : 1||NCA full cell exhibits two distinct peaks (~2.1 V for LTO and ~3.0 V for SnSb) at cycle 5. After 100 cycles, the higher-voltage SnSb peaks diminish while the LTO peak remains stable, suggesting the primary degradation mechanism in the LTO : SnSb blended anode is alloying-related degradation of the SnSb. For the 8 : 2||NCA cell, a similar trend is observed but with an additional shift in the LTO peak (~2.1 V → ~2.2 V), indicating significant aging of LTO due to SnSb-induced volume expansion and pulverization. This shift in the voltage for LTO-based cells corroborates prior reports that investigated aging behavior under various scenarios, particularly under high-rate conditions (*i.e.* >1C), and their d*Q*/d*V* analyses show that the surface of the anode showed signs of fracture.[58,59] This effect becomes more apparent in full cells comprising >30% SnSb (Fig. S7), where the higher-voltage SnSb peak nearly disappears after 100 cycles, leaving behind two peaks at ~2.5 V, signaling a significant electrochemical transformation of the blended anode. For the 3 : 7||NCA full cell, severe degradation leads to

Table 2 Summary of full-cell electrochemical properties (average discharge potential and discharge capacity) of LTO : SnSb electrodes paired with NCA with the following ratios: 10 : 0, 9 : 1, 8 : 2, 7 : 3, 5 : 5, 3 : 7 (wt : wt LTO : SnSb)

LTO : SnSb mass ratio (wt : wt)	Average discharge voltage (V)	C/10 capacity[a] (mAh g^{-1})	C/5 capacity[a] (mAh g^{-1})	C/2 capacity[a] (mAh g^{-1})	1C capacity[a] (mAh g^{-1})	2C capacity[a] (mAh g^{-1})	Specific energy[b] (Wh kg^{-1})
10 : 0	2.11	180.5	172.9	158.6	146.5	131.0	213.5
9 : 1	2.43	250.6	242.9	225.9	210.9	193.4	294.2
8 : 2	2.62	296.1	287	268.8	251.3	230.7	351.4
7 : 3	2.73	387.7	371.9	345.6	318.0	284.3	397.1
5 : 5	2.79	485.9	474.8	451.6	421.9	384.6	424.8
3 : 7	2.83	637.3	624.7	592.3	554.8	502.6	453.3

[a] Capacities normalized by the anode active material mass. [b] Specific energy normalized to both total anode and cathode mass (including carbon and binder), not including current collector, electrolyte, and packaging.

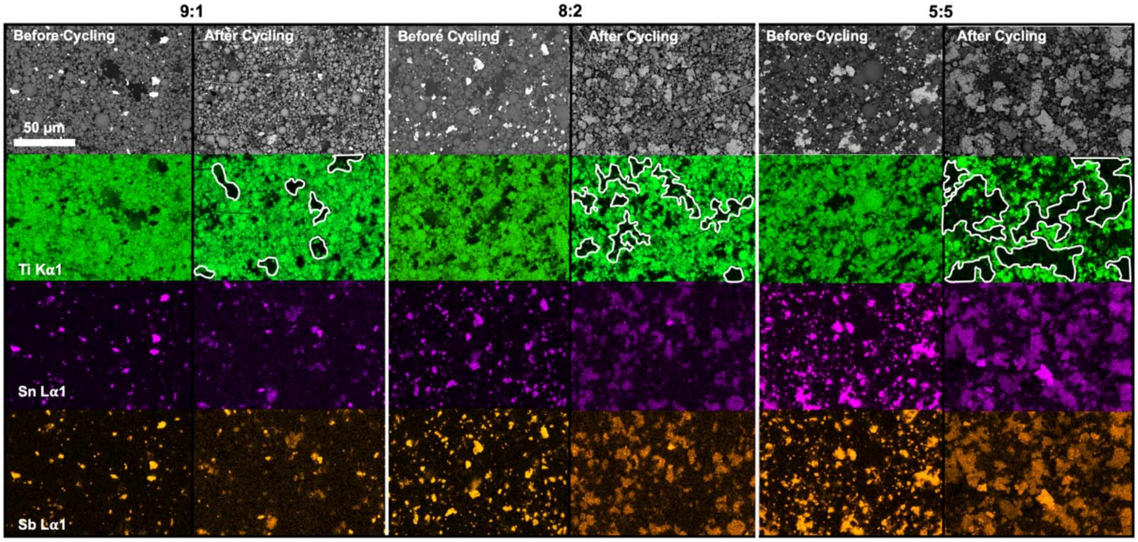

Fig. 4 Scanning electron micrographs and energy dispersive spectroscopy (EDS) maps (Ti, Sn, and Sb) of pre- and post-mortem 9 : 1, 8 : 2, and 5 : 5 LTO : SnSb blended anodes after 100 cycles at C/2. The white traces in the Ti energy dispersive spectroscopy maps outline the network of LTO particles after cycling.

a near complete loss of blended anode capacity, with no distinguishable dQ/dV peaks after 100 cycles. This further confirms the detrimental impact of excessive SnSb content on long-term cycle stability of the LTO : SnSb blended anode.

We hypothesize that the capacity degradation of the LTO : SnSb blended anodes with >30 wt% SnSb was primarily due to the inherent volume expansion and pulverization of SnSb, while the lack of degradation for LTO : SnSb blended anodes with <20 wt% SnSb may be attributed to the presence of a more compact LTO network surrounding the SnSb material, thus potentially mitigating significant pulverization, which is the subject of future studies. To investigate this, SEM, coupled with energy dispersive spectroscopy (EDS) for chemical mapping of the anodes (Fig. 4), was conducted on pre- and post-cycled samples of 9 : 1, 8 : 2, and 5 : 5 LTO : SnSb blended anodes after 100 cycles at C/2. Additional SEM/EDS micrographs and EDS elemental maps for all blended anodes are available in the SI (Fig. S8–S14). As expected, for the 10 : 0 anode (100% LTO), SEM images (Fig. S8) reveal a compact, dense anode layer. In contrast, SnSb naturally forms a rougher, more porous network (Fig. S9). For the 9 : 1 anode, the Ti EDS map shows a near-continuous film on the electrode surface before cycling; after 100 cycles, minimal surface changes are observed and the visible SnSb particles retain their original size. However, in the 8 : 2 anode, two distinct changes emerge: (i) before cycling, the LTO network appears well-structured, but after 100 cycles, a larger LTO particle network develops; and (ii) the SnSb particles pulverizes, resulting in smaller aggregates of the original SnSb powder after 100 cycles. This effect is more pronounced in the 5 : 5 anode, where the LTO network becomes significantly disrupted and there is a greater presence of pulverized SnSb particles after 100 cycles. This behavior aligns with observations from the 0 : 10 anode (100% SnSb), where extensive SnSb pulverization is clearly visible after cycling (Fig. S9). This pulverization behavior of alloying anodes (*e.g.*, Sn, SnSb, and Sb) is consistent with prior investigations that probed deeper into understanding the effects of performance degradation in SnSb,[60] and mitigations therein with nanoporous forms of Sn and SnSb.[43,44] These findings suggest that limiting the SnSb content <20 wt% is crucial for long-term LTO : SnSb blended anode stability, consistent with the dQ/dV analyses. Notably, the combination of the dQ/dV analyses and SEM/EDS provides only cursory insight, and in future studies, techniques such as *operando* X-ray micro-computed tomography and transmission X-ray microscopy can reveal a more quantitative interpretation of this degradation behavior in composite anodes with high spatial resolution.

In this study, we developed and demonstrated a blended anode concept that combines zero-strain LTO, an oxide-based anode material, with high-capacity SnSb, which operates *via* alloying. By systematically varying the LTO-to-SnSb mass ratios, we found that maintaining the SnSb content below 20 wt% enables high specific capacities (250–350 mAh g^{-1}) at average full-cell discharge voltages of 2.43–2.62 V, while achieving excellent cycle retention (>80% after 100 cycles at C/2 rates). This strategy highlights a technologically-relevant pathway for seamless integration into existing lithium-ion battery manufacturing processes. Future research focusing on carbon electrode architecture design, such as high-areal-capacity carbon,[61–63] can further extend the cycle life of alloying anodes, advancing the practical viability of this emerging blended anode concept.

Author contributions

S. A. L.: writing – original draft, analyses, conceptualization, experimental. C. A. M.: analyses, experimental. T. H.: analyses, review and editing. J. S. K.: supervision, conceptualization, writing – original draft, review and editing.

Conflicts of interest

The authors declare no competing financial interest.

Data availability

Data related to this work are presented in the main manuscript and the SI. Additional relevant data are available from the corresponding author upon reasonable request.

Experimental details; estimated gravimetric and volumetric energy densities; additional half-cell charge–discharge voltage profiles; additional half-cell rate capability data; upper voltage limit cutoff; N : P ratio optimization; additional full-cell charge–discharge voltage profiles; dQ/dV analyses; additional scanning electron micrographs and energy dispersive spectroscopy elemental maps. See DOI: **https://doi.org/10.1039/d5ta05287d**.

Acknowledgements

The authors gratefully acknowledge support from the Office of Naval Research under NAVSEA contract N00024-13-D-6400. This paper describes objective technical results and analyses. Any subjective views of opinions that might be expressed in the paper do not necessarily represent the views of the U.S. Department of Defense or the U.S. Government. The authors also thank Dr Konstantinos Gerasopoulos for insightful discussions and Dr Ann Choi for assistance with scanning electron microscopy.

References

1 M. N. Obrovac and V. L. Chevrier, Alloy negative electrodes for Li-ion batteries, *Chem. Rev.*, 2014, **114**, 11444–11502.

2 S. V. Gopinadh, P. V. R. L. Phanendra, A. V, B. John and M. TD, Progress, challenges, and perspectives on alloy-based anode materials for lithium ion battery: A mini-review, *Energy Fuels*, 2024, **38**, 17253–17277.

3 M. Peng, K. Shin, L. Jiang, Y. Jin, K. Zeng, X. Zhou and Y. Tang, Alloy-type anodes for high-performance rechargeable batteries, *Angew. Chem., Int. Ed.*, 2022, **61**, e202206770.

4 D. Larcher, S. Beattie, M. Morcrette, K. Edström, J.-C. Jumas and J.-M. Tarascon, Recent findings and prospects in the field of pure metals as negative electrodes for Li-ion batteries, *J. Mater. Chem. A*, 2007, **17**, 3759–3772.

5 S. Liang, Y.-J. Cheng, J. Zhu, Y. Xia and P. Müller-Buschbaum, A chronicle review of nonsilicon (Sn, Sb, Ge)-based lithium/sodium-ion battery alloying anodes, *Small*, 2020, **4**, 2000218.

6 J. Asenbauer, T. Eisenmann, M. Kuenzel, A. Kazzazi, Z. Chen and D. Bresser, The success story of graphite as a lithium-ion anode material – fundamentals, remaining challenges, and recent developments including silicon (oxide) composites, *Sustainable Energy Fuels*, 2020, **4**, 5387–5416.

7 W.-J. Zhang, A review of the electrochemical performance of alloy anodes for lithium-ion batteries, *J. Power Sources*, 2011, **196**, 13–24.

8 J. S. Ko, B. Tan, M. W. Logan, S. A. Langevin and K. Gerasopoulos, Chemical pre-lithiation of $LiMn_2O_4$ balances the low first cycle efficiency of silicon anodes, *J. Mater. Chem. A*, 2024, **12**, 14354–14359.

9 C. P. Sandhya, B. John and C. Gouri, Lithium titanate as anode material for lithium-ion cells: A review, *Ionics*, 2014, **20**, 601–620.

10 H. Yan, D. Zhang, Qilu, X. Duo and X. Sheng, A review of spinel lithium titanate ($Li_4Ti_5O_{12}$) as electrode material for advanced energy storage devices, *Ceram. Int.*, 2021, **47**, 5870–5895.

11 H. Ding, Z. Song, H. Zhang, H. Zhang and X. Li, Niobium-based oxide anodes toward fast and safe energy storage: A review, *Mater. Today Nano*, 2020, **11**, 100082.

12 K. J. Griffith, Y. Harada, S. Egusa, R. M. Ribas, R. S. Monteiro, R. B. Von Dreele, A. K. Cheetham, R. J. Cava, C. P. Grey and J. B. Goodenough, Titanium niobium oxide: From discovery to application in fast-charging lithium-ion batteries, *Chem. Mater.*, 2021, **33**, 4–18.

13 D. W. Murphy, R. J. Cava, S. M. Zahurak and A. Santoro, Ternary Li_xTiO_2 phases from insertion reactions, *Solid State Ionics*, 1983, **9–10**, 413–417.

14 A. Salvatore Aricò, P. Bruce, B. Scrosati, J.-M. Tarascon and W. van Schalkwijk, Nanostructured materials for advanced energy conversion and storage devices, *Nat. Mater.*, 2005, **4**, 366–377.

15 D. Dambournet, I. Belharouak and K. Amine, Tailored preparation methods of TiO_2 anatase, rutile, brookite: Mechanism of formation and electrochemical properties, *Chem. Mater.*, 2010, **22**, 1173–1179.

16 A. G. Dylla, G. Henkelman and K. J. Stevenson, Lithium insertion in nanostructured TiO_2(B) architectures, *Acc. Chem. Res.*, 2013, **46**, 1104–1112.

17 N. Takami, H. Inagaki, T. Kishi, Y. Harada, Y. Fujita and K. Hoshina, Electrochemical kinetics and safety of 2-volt class Li-ion battery system using lithium titanium oxide anode, *J. Electrochem. Soc.*, 2008, **156**, A128.

18 B. Zhao, R. Ran, M. Liu and Z. Shao, A comprehensive review of $Li_4Ti_5O_{12}$-based electrodes for lithium-ion batteries: The latest advancements and future perspectives, *Mater. Sci. Eng., R*, 2015, **98**, 1–71.

19 Z. Chen, I. Belharouak, Y.-K. Sun and K. Amine, Titanium-based anode materials for safe lithium-ion batteries, *Adv. Funct. Mater.*, 2012, **23**, 959–969.

20 Toshiba, *Toshiba Rechargeable Battery SCiB*, **https://www.global.toshiba/content/dam/toshiba/ww/products-solutions/battery/scib/pdf/ToshibaRechargeableBattery-en.pdf**.

21 C. Peng, S. Liang, Y. Yu, L. Cao, C. Yang, X. Liu, K. Guo, P. Muller-Büschbaum, Y.-J. Cheng and C. Wang, A chronicle of titanium niobium oxide materials for high-performance lithium-ion batteries: From laboratory to industry, *Carbon Neutralization*, 2024, **3**, 1036–1091.

22 N. Takami, K. Ise, Y. Harada, T. Iawasaki, T. Kishi and K. Hoshina, High-energy, fast-charging, long-life lithium-ion batteries using $TiNb_2O_7$ anodes for automotive applications, *J. Power Sources*, 2018, **396**, 429–436.

23 Y. Sheng, Y. Wang, S. Yin, L. Zhao, X. Zhang, D. Liu and G. Wen, Niobium-based oxide for anode materials for lithium-ion batteries, *Chem.–Eur. J.*, 2013, **30**, e202302865.

24 V. Augustyn, J. Come, M. A. Lowe, J. W. Kim, P.-L. Taberna, S. H. Tolbert, H. D. Abruña, P. Simon and B. Dunn, High-rate electrochemical energy storage through Li^+ intercalation pseudocapacitance, *Nat. Mater.*, 2013, **12**, 518–522.

25 E. A. Pogue, S. A. Langevin, T. Hamann, K. K. Rao, M. A. Schroeder, N. Q. Le, C. McHale, Z. Burchfield and J. S. Ko, Enhancing low-temperature lithium-ion battery performance under high-rate conditions with niobium oxides, *Mater. Today Energy*, 2024, **45**, 101663.

26 L. Sun, Y. Liu, R. Shao, J. Wu, R. Jiang and Z. Jin, Recent progress and future perspective on practical silicon anode-based lithium ion batteries, *Energy Storage Mater.*, 2022, **46**, 482–502.

27 K. Feng, M. Li, W. Liu, A. Ghorbani Kashkooli, X. Xiao, M. Cai and Z. Chen, Silicon-based anodes for lithium-ion batteries: From fundamentals to practical applications, *Small*, 2018, **14**, 1702737.

28 X. Zuo, J. Zhu, P. Müller-Buschbaum and Y.-J. Cheng, Silicon based lithium-ion battery anodes: A chronicle perspective review, *Nano Energy*, 2017, **31**, 113–143.

29 M. Jiang, J. Chen, Y. Zhang, N. Song, W. Jiang and J. Yang, Assembly: A key enabler for the construction of superior silicon-based anodes, *Adv. Sci.*, 2022, **9**, 2203162.

30 P. Li, H. Kim, S.-T. Myung and Y.-K. Sun, Diverting exploration of silicon anode into practical way: A review focused on silicon-graphite composite for lithium ion batteries, *Energy Storage Mater.*, 2021, **35**, 550–576.

31 S. He, S. Huang, S. Wang, I. Mizota, X. Liu and X. Hou, Considering critical factors of silicon/graphite anode materials for practical high-energy lithium-ion battery applications, *Energy Fuels*, 2021, **35**, 944–964.

32 J. Wu, Y. Cao, H. Zhao, J. Mao and Z. Guo, The critical role of carbon in marrying silicon and graphite anodes for high-energy lithium-ion batteries, *Carbon Energy*, 2019, **1**, 57–76.

33 M. Gautam, G. K. Mishra, K. Bhawana, C. S. Kalwar, D. Dwiveldi, A. Yadav and S. Mitra, Relationship between silicon percentage in graphite anode to achieve high-energy-density lithium-ion batteries, *ACS Appl. Mater. Interfaces*, 2024, **16**, 45809–45820.

34 Z. Yan, S. Yi, X. Li, J. Jiang, D. Yang and N. Du, A scalable silicon/graphite anode with high silicon content for high-energy lithium-ion batteries, *Mater. Today Energy*, 2023, **31**, 101225.

35 M. Winter and J. O. Besenhard, Electrochemical lithiation of tin and tin-based intermetallics and composites, *Electrochim. Acta*, 1999, **45**, 31–50.

36 A. Trifonova, M. Wachtler, M. Winter and J. O. Besenhard, Sn-Sb and Sn-Bi alloys as anode materials for lithium-ion batteries, *Ionics*, 2002, **8**, 321–328.

37 J. S. Ko, K. Gerasopoulos and M. W. Logan, High capacity blended anodes for Li-ion batteries, *US Pat.*, 18209290, 2023.

38 K. Mukai, Y. Kato and H. Nakano, Understanding the zero-strain lithium insertion scheme of $Li[Li_{1/3}Ti_{5/3}]O_4$: Structural changes at atomic scale clarified by Raman spectroscopy, *J. Phys. Chem. C*, 2014, **118**, 2992–2999.

39 J. Sturman, Y. Zhang, C.-H. Yim, S. Niketic, M. Toupin, E. A. Baranova and Y. Abu-Lebdeh, Composites of silicon@$Li_4Ti_5O_{12}$ and graphite for high-capacity lithium-ion battery anode materials, *J. Electrochem. Soc.*, 2021, **168**, 010524.

40 R. Cai, X. Yu, X. Liu and Z. Shao, $Li_4Ti_5O_{12}$/Sn composite anodes for lithium-ion batteries: Synthesis and electrochemical performance, *J. Power Sources*, 2010, **195**(24), 8244–8250.

41 A. K. Haridas, C. S. Sharma and T. N. Rao, Electrospun SnO_2/LTO composite sub-micron dimpled spheres as high performance anode material for lithium ion batteries, *ECS Trans.*, 2017, **77**(11), 339–347.

42 J. Yang, M. Wachtler, M. Winter and J. O. Besenhard, Sub-microcrystalline Sn and Sn-SnSb powders as lithium storage materials for lithium-ion batteries, *Electrochem. Solid-State Lett.*, 1999, **2**(4), 161–163.

43 J. B. Cook, E. Detsi, Y. Liu, Y.-L. Liang, H.-S. Kim, X. Petrissans, B. Dunn and S. H. Tolbert, Nanoporous tin with a granular hierarchical ligament morphology as a highly stable Li-ion battery anode, *ACS Appl. Mater. Interfaces*, 2017, **9**, 293–303.

44 T. C. Lin, A. Dawson, S. C. King, Y. Yan, D. S. Ashby, J. A. Msazzetti, B. S. Dunn, J. Nelson Weker and S. H. Tolbert, Understanding stabilization in nanoporous intermetallic alloy anodes for Li-ion batteries using operando transmission X-ray microscopy, *ACS Nano*, 2020, **14**, 14820–14830.

45 Q. Sang, S. Hao, J. Han and Y. Ding, Dealloyed nanoporous materials for electrochemical energy conversion and storage, *EnergyChem*, 2022, **4**, 100069.

46 X. Dong, W. Liu, X. Chen, J. Yan, N. Li, S. Shi, S. Zhang and X. Yang, Novel three dimensional hierarchical porous Sn-Ni alloys as anode for lithium ion batteries with long cycle life by pulse electrodeposition, *Chem. Eng. J.*, 2018, **350**, 791–798.

47 W. Li, X. Guo, Y. Lu, L. Wang, A. Fan, M. Sui and H. Yu, Amorphous nanosized silicon with hierarchically porous structure for high-performance lithium ion batteries, *Energy Storage Mater.*, 2017, **7**, 203–208.

48 S. Guo, Z. Sun, Y. Liu, X. Guo, H. Feng, S. Lui, C. Wei, Y. Zheng, X. Zhang, K. Kim, H. Liu, P. K. Chu and B. Gao, Multiscale micro-nano hierarchical porous germanium with self-adaptive stress dispersion for highly robust lithium-ion batteries anode, *Adv. Energy Mater.*, 2024, **14**, 2303876.

49 Y. Yao, N. Liu, M. T. McDowell, M. Pasta and Y. Cui, Improving the cycling stability of silicon nanowire anodes with conducting polymer coatings, *Energy Environ. Sci.*, 2012, **5**, 7927–7930.

50 L.-F. Cui, R. Ruffo, C. K. Chan, H. Peng and Y. Cui, Crystalline-amorphous core-shell silicon nanowires for high capacity and high current battery electrodes, *Nano Lett.*, 2009, **9**, 491–495.

51 T. D. Bogart, D. Oka, X. Lu, M. Gu, C. Wang and B. A. Korgel, Lithium ion battery performance of silicon nanowires with carbon skin, *ACS Nano*, 2014, **8**, 915–922.

52 C. K. Chan, R. N. Patel, M. J. O'Connell, B. A. Korgel and Y. Cui, Solution-grown silicon nanowires for lithium-ion battery anodes, *ACS Nano*, 2010, **4**, 1443–1450.

53 Y. Luo, Y. Chen, N. Koratkar and W. Liu, Densification of alloying anodes for high energy lithium-ion batteries: Critical perspective on inter- versus intra-particle porosity, *Adv. Sci.*, 2024, **11**, 2403530.

54 A. J. Smith, J. C. Burns and J. R. Dahn, High-precision differential capacity analysis of $LiMn_2O_4$/graphite cells, *Electrochem. Solid-State Lett.*, 2011, **14**, A39–A41.

55 A. J. Smith and J. R. Dahn, Delta differential capacity analysis, *J. Electrochem. Soc.*, 2012, **159**, A290–A293.

56 A. J. Smith, H. M. Dahn, J. C. Burns and J. R. Dahn, Long-term low-rate cycling of $LiCoO_2$/graphite Li-ion cells at 55° C, *J. Electrochem. Soc.*, 2012, **159**, A705–A710.

57 H. M. Dahn, A. J. Smith, J. C. Burns, D. A. Stevens and J. R. Dahn, User-friendly differential voltage analysis freeware for the analysis of degradation mechanisms in Li-ion batteries, *J. Electrochem. Soc.*, 2012, **159**, A1405–A1409.

58 X. Zhang, Z. Shi, H. Zhang and S. Dong, Degradation analysis of $Li_4Ti_5O_{12}$ of lithium-ion battery under tram operating conditions, *IEEE Trans. Transp. Electrif.*, 2025, **11**, 1.

59 C. Wang, Z. Liu, Y. Sun, Y. Gao and P. Yan, Aging behavior of lithium titanate battery under high-rate discharging cycle, *Energies*, 2021, **14**, 5482.

60 A. T. Tesfaye, Y. D. Yücel, M. K. S. Barr, L. Santinacci, F. Vacandio, F. Dumur, S. Maria, L. Monconduit and T. Djenizian, The electrochemical behavior of SnSb as an anode for Li-ion batteries studied by electrochemical impedance spectroscopy and electron microscopy, *Electrochim. Acta*, 2017, **256**, 155–161.

61 G. Li, T. Ouyang, T. Xiong, Z. Jiang, D. Adekoya, Y. Wu, Y. Huang and M.-S. Balogun, All-carbon-frameworks enabled thick electrode with exceptional high-areal-capacity for Li-ion storage, *Carbon*, 2021, **174**, 1–9.

62 S. Zhou, P. Huang, T. Xiong, F. Yang, H. Yang, Y. Huang, D. Li, J. Deng and M.-S. Balogun, Sub-thick electrodes with enhanced transport kinetics via in situ epitaxial heterogeneous interfaces for high areal-capacity lithium ion batteries, *Small*, 2021, **17**(26), 2100778.

63 H. Yang, T. Xiong, Z. Zhu, R. Xiao, X. Yao, Y. Huang and M.-S. Balogun, Deciphering the lithium storage chemistry in flexible carbon fiber-based self-supportive electrodes, *Carbon Energy*, 2022, **4**(5), 820–832.